LETTER

doi:10.1038/nature25776

Measurement of Jupiter's asymmetric gravity field

L. Iess[1], W. M. Folkner[2], D. Durante[1], M. Parisi[2], Y. Kaspi[3], E. Galanti[3], T. Guillot[4], W. B. Hubbard[5], D. J. Stevenson[6], J. D. Anderson[7], D. R. Buccino[2], L. Gomez Casajus[8], A. Milani[9], R. Park[2], P. Racioppa[1], D. Serra[9], P. Tortora[8], M. Zannoni[8], H. Cao[6], R. Helled[10], J. I. Lunine[11], Y. Miguel[4], B. Militzer[12], S. Wahl[12], J. E. P. Connerney[13], S. M. Levin[2] & S. J. Bolton[7]

The gravity harmonics of a fluid, rotating planet can be decomposed into static components arising from solid-body rotation and dynamic components arising from flows. In the absence of internal dynamics, the gravity field is axially and hemispherically symmetric and is dominated by even zonal gravity harmonics J_{2n} that are approximately proportional to q^n, where q is the ratio between centrifugal acceleration and gravity at the planet's equator[1]. Any asymmetry in the gravity field is attributed to differential rotation and deep atmospheric flows. The odd harmonics, J_3, J_5, J_7, J_9 and higher, are a measure of the depth of the winds in the different zones of the atmosphere[2,3]. Here we report measurements of Jupiter's gravity harmonics (both even and odd) through precise Doppler tracking of the Juno spacecraft in its polar orbit around Jupiter. We find a north–south asymmetry, which is a signature of atmospheric and interior flows. Analysis of the harmonics, described in two accompanying papers[4,5], provides the vertical profile of the winds and precise constraints for the depth of Jupiter's dynamical atmosphere.

The external, harmonic, gravitational potential of a body can be expanded into a series of complex spherical harmonic functions $Y_{lm}(\theta,\phi)$ (an orthonormal basis for functions defined on the unit sphere, with each element defined by its degree l and order m), multiplied by a scaling factor that depends on the normalized radial distance r/R from the centre of the body:

$$U(r,\theta,\varphi) = -\frac{GM}{r}\left[1+\sum_{l\geq 2}\left(\frac{R}{r}\right)^l \sum_{m=-l}^{l} U_{lm}Y_{lm}(\theta,\varphi)\right]$$

where GM is the gravitational parameter. For a planet, R is generally chosen as the equatorial radius of the body. Were the internal density ρ of the body known, the harmonic coefficients U_{lm} could be obtained from the integral over the volume V of the body (see ref. 6 and references therein):

$$U_{lm} = \frac{1}{(2l+1)MR^l}\int_V (r')^l Y^*_{lm}(\theta',\varphi')\rho(r',\theta',\varphi')\mathrm{d}V'$$

When the density does not depend on longitude, as expected for a fluid and rapidly rotating planet such as Jupiter, the above expression can be simplified:

$$J_l \equiv -\sqrt{\{2l+1\}}\,U_{l0} = -\frac{1}{MR^l}\int_V (r')^l P_l(\theta')\rho(r',\theta')\mathrm{d}V'$$

where P_l is the Legendre polynomial of degree l. Thus, the zonal coefficients J_l bear important, although non-unique, information about the density distribution inside Jupiter.

On 4 July 2016, the Juno spacecraft was captured by the gravity field of Jupiter, starting its prime mission—the investigation of the deep interior, the magnetosphere and the atmosphere of the planet. The spacecraft is currently in a highly eccentric (eccentricity $e = 0.98$), long-period (52.9 days) polar orbit, with a pericentre altitude of about 4,000 km above the 1-bar level, as inferred from radio occultations[7].

As a consequence of the equivalence principle, gravity field determinations require the measurement of the relative motion of (at least) two masses. In the Juno gravity experiment, the spacecraft acts as a test particle falling in the gravity field of the planet. Earth is the second end mass. Jupiter's gravity is inferred from range-rate measurements between a ground antenna and the spacecraft during perijove passes. To measure Jupiter's gravity field, the ground station transmits two carrier signals, at 7,153 MHz (X band) and 34,315 MHz (Ka band). On board, an X-band transponder and a dedicated Ka-band frequency translator (a radio-science instrument) lock the incoming carrier signals and retransmit them back to the ground station at 8,404 MHz and 32,088 MHz, respectively. The range-rate (Doppler) observable is obtained by comparing the transmitted and received frequencies. Juno is the first deep-space mission that uses Ka-band radio systems for planetary geodesy. The Ka-band and multi-frequency radio links have previously been used only for precision tests of relativistic gravity in the cruise phase of the Cassini spacecraft[8,9]. Owing to the dispersion properties of plasmas, Ka-band radio links provide excellent immunity to the adverse effects of charged particles along the propagation path, including the Io torus (a potential source of bias in the gravity estimates; see Methods). The Juno radio system enables further reduction of plasma noise (an additional approximately 75%) by combining X- and Ka-band Doppler observables[10]. To reduce the noise from tropospheric water vapour, a radiometer placed near the ground antenna continuously monitors the wet path delay along the line of sight.

Our analysis is based on the first two Ka-band perijove passes of Juno, labelled PJ3 (11 December 2016) and PJ6 (19 May 2017). Doppler measurements were integrated over 60 s before processing to enable adequate sampling of the gravity signal. At this timescale, the measured two-way range-rate noise in the Ka band was 1.5×10^{-5} m s^{-1} for an integration time of 60 s, in line with the expectations from Ka-band radio link noise models[11]. The Doppler noise is approximately white between 4×10^{-4} Hz and 2×10^{-2} Hz (the characteristic frequency range of the gravity signal).

The dynamical model used in the orbital fit is driven by the theoretical expectations for the gravity field of gaseous planets. We adopt here the standard spherical harmonics representation of planetary gravity fields, whose expansion coefficients are determined by the density distribution inside the body (ref. 6 and references therein). Models of Jupiter's interior structure predict that the planet's gravity is dominated by an axially and hemispherically symmetric component attributed to solid-body rotation[12,13]. This component is determined by the radial density distribution in the rotating planet and is represented by even zonal harmonic coefficients $J_{2n}\propto q^n$. Atmospheric and internal dynamics can produce small density perturbations that result in a more complex gravity representation, involving

[1]Sapienza Università di Roma, 00184 Rome, Italy. [2]Jet Propulsion Laboratory, California Institute of Technology, Pasadena, California 91109, USA. [3]Weizmann Institute of Science, Rehovot 76100, Israel. [4]Observatoire de la Côte d'Azur, 06304 Nice, France. [5]Lunar and Planetary Laboratory, University of Arizona, Tucson, Arizona 85721, USA. [6]California Institute of Technology, Pasadena, California 91125, USA. [7]Southwest Research Institute, San Antonio, Texas 78238, USA. [8]Università di Bologna, 47100 Forlì, Italy. [9]Università di Pisa, 56127 Pisa, Italy. [10]University of Zurich, 8057 Zurich, Switzerland. [11]Cornell University, Ithaca, New York 14853, USA. [12]University of California, Berkeley, California 94720, USA. [13]NASA Goddard Space Flight Center, Greenbelt, Maryland 20771, USA.

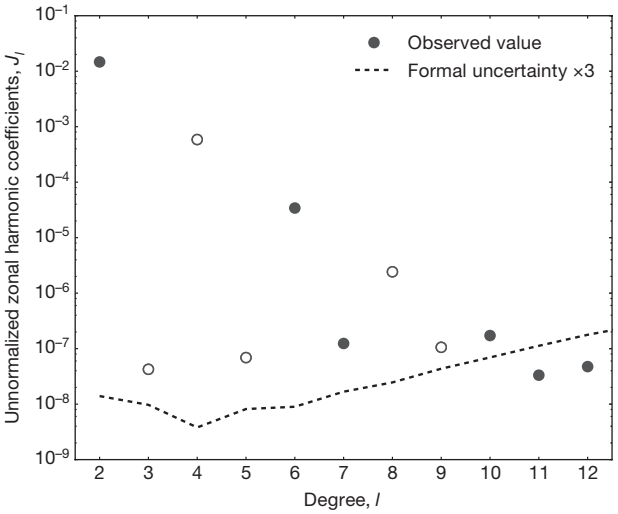

Figure 1 | Zonal gravity harmonic coefficients J_2–J_{12}. The dashed line shows the realistic uncertainty (Table 1). Solid and empty circles denote positive and negative values, respectively.

Table 1 | Gravity solution

	Value	Uncertainty
J_2 ($\times 10^{-6}$)	14,696.572	0.014
C_{21} ($\times 10^{-6}$)	−0.013	0.015
S_{21} ($\times 10^{-6}$)	−0.003	0.026
C_{22} ($\times 10^{-6}$)	0.000	0.008
S_{22} ($\times 10^{-6}$)	0.000	0.011
J_3 ($\times 10^{-6}$)	−0.042	0.010
J_4 ($\times 10^{-6}$)	−586.609	0.004
J_5 ($\times 10^{-6}$)	−0.069	0.008
J_6 ($\times 10^{-6}$)	34.198	0.009
J_7 ($\times 10^{-6}$)	0.124	0.017
J_8 ($\times 10^{-6}$)	−2.426	0.025
J_9 ($\times 10^{-6}$)	−0.106	0.044
J_{10} ($\times 10^{-6}$)	0.172	0.069
J_{11} ($\times 10^{-6}$)	0.033	0.112
J_{12} ($\times 10^{-6}$)	0.047	0.178
k_{22}	0.625	0.063
α (°)	268.0570	0.0013
δ (°)	64.4973	0.0014

Jupiter's gravity harmonics coefficients (unnormalized; reference radius 71,492 km), the Love number k_{22} and the pole coordinates (α, right ascension; δ, declination) at epoch J2017.0, obtained from the PJ3 and PJ6 Juno science orbits. The deviation of the principal axis of inertia from the spin axis, as inferred from the uncertainty in $C_{21}=\mathrm{Re}(U_{21})\sqrt{5/3}$ and $S_{21}=\mathrm{Im}(U_{21})\sqrt{5/3}$, is smaller than about 0.4 arcsec (130 m at the reference radius). J_2 includes a tidal term currently estimated at about 2.98×10^{-8}. The associated uncertainties are realistic values that can be used for analysis and interpretation and correspond to three times the formal 1σ uncertainties.

odd zonal and possibly tesseral harmonics, as well as small corrections to the even zonal harmonics[3,5,14]. The latter are however indiscernible from the much larger contribution of solid-body rotation up to harmonics of degree 12, where the dynamics is expected to dominate the gravity signal[2]. Hence, any detection of an asymmetric (hemispherically or axially) gravity field would be a signature of internal dynamics due to flows. Juno tracking data have provided evidence of hemispherical (north–south) asymmetries in the gravity field of a giant planet.

Prior to PJ3, the best estimate of Jupiter's even zonal gravity field was obtained using noisier X-band Doppler observables from the first two Juno perijove passes (PJ1 and PJ2)[15,16]. These early results improved previous estimates[17,18] of the zonal harmonic coefficients J_4 and J_6 and allowed the determination of J_8. Those measurements of J_4 and J_6 have been used to constrain the radial density profile of the planet[19]. However, the magnitude of the much smaller odd zonal field could not be determined, because of the unfavourable observation geometry and the large propagation noise caused by interplanetary plasma on the X-band uplink signal (7.2 GHz).

High-accuracy Ka-band data acquired during PJ3 and PJ6 provided the first estimate of the asymmetric component of Jupiter's gravity (Fig. 1 and Table 1). We processed Doppler data using orbit determination codes developed for spacecraft navigation (the MONTE software of the Jet Propulsion Laboratory) and an external estimation filter. Data from PJ3 and PJ6 were separately fitted with the spacecraft state vector at the beginning of the tracking pass (about 6 h before transit at the pericentre), Jupiter's gravitational parameter GM, the zonal harmonic coefficients J_2–J_{24}, the tesseral quadrupole harmonics, the pole position and rate at epoch J2017.0 (1 January 2017, 12:00 UTC) and the k_{22} Love number. This set of parameters allows the fitting of all data to the noise level. The $l=2$ tesseral coefficients, although not strictly required for a least-size solution, were estimated to search for a possible deviation of the principal axis of inertia from the spin axis. We adopted the masses and the ephemerides of the Jovian satellites from file[18] jup310 of NASA's Navigation and Ancillary Information Facility and considered their uncertainties in the final covariance matrix. A linear correction to Jupiter's orbit was applied to fit range data acquired in the X band during the tracking pass. The relativistic Lense–Thirring precession was included and the magnitude of Jupiter's polar moment of inertia was set to interior model predictions, considered with 20% of uncertainty (affecting the recovery of Jupiter's spin axis). The single-arc solutions were then combined in a global multi-arc solution made up by two categories of parameters: local (pertaining to each arc) and global (common to both arcs). Only the initial spacecraft conditions were treated as local parameters. No constraints were applied to the global parameters, except Jupiter's gravitational parameter, whose current estimate is more accurate than that obtained so far from Juno (see Methods). The data were weighted according to the Doppler noise in each Ka-band pass, assuming no correlation between samples. The correctness of this assumption was verified a posteriori from the nearly white power spectral density of the residuals in the frequency band of interest (see Methods).

The two single-arc gravity solutions are fully compatible at 2σ, except for J_4 (3.5σ; see Fig. 2 for examples). Fitting PJ3 and PJ6 data jointly does

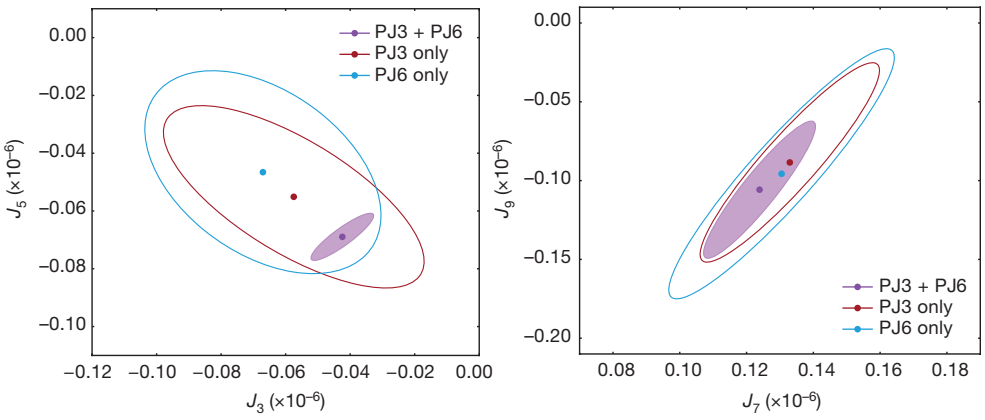

Figure 2 | 3σ uncertainty ellipses of J_3–J_5 and J_7–J_9. Brown and cyan ellipses represent single-arc PJ3 and PJ6 solutions, respectively. The solid violet ellipse shows the PJ3 + PJ6 combined solution.

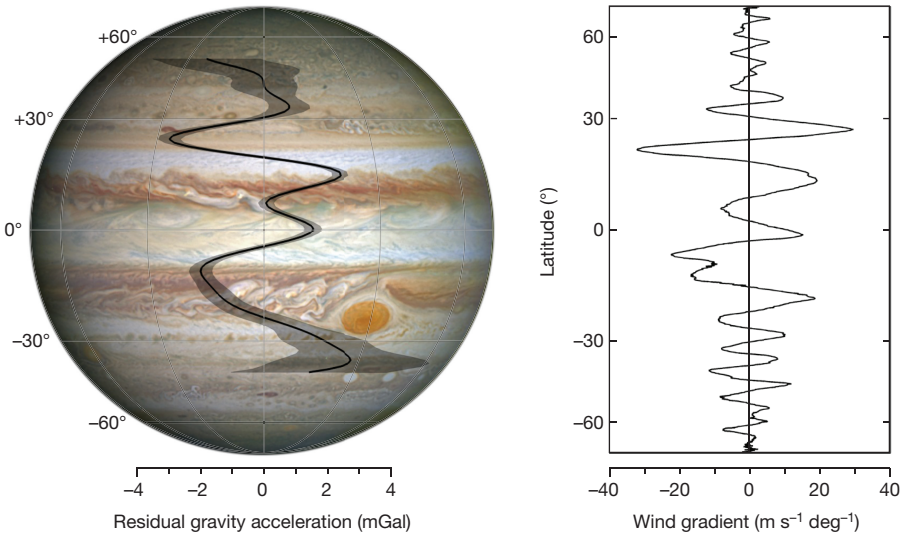

Figure 3 | Gravity disturbances due to atmospheric dynamics. a, An image of Jupiter taken by the Hubble Wide Field Camera in 2014 (https://en.wikipedia.org/wiki/Jupiter), showing the latitudinal dependence of residual gravity acceleration (in milligals, positive outwards) and associated 3σ uncertainty (shaded area) at a reference distance of 71,492 km, when the gravity from the even zonal harmonics J_2, J_4, J_6 and J_8 is removed. The residual gravity field, which is dominated by the dynamics of the flows, shows marked peaks correlated with the band structure. **b**, Latitudinal gradient of the measured wind profile. The largest (negative) peak of -3.4 ± 0.4 mGal (3σ) is found at a latitude of 24° N, where the latitudinal gradient of the wind speed reaches its largest value. The relation between the gravity disturbances and wind gradients is discussed in an accompanying paper[4].

not require any tesseral components other than the quadrupole, even if the two ground tracks are separated by about 150°. However, the available data do not allow us to set a reliable upper limit to tesseral harmonics, although numerical simulations indicate that a tesseral field corresponding to a flow depth larger than 380 km would produce signatures in the Doppler residuals (see Methods and ref. 20). The consider covariances that correspond to this flow depth are larger than the uncertainties reported in Table 1. The current dataset does not show evidence of a time-varying gravity field, as may result from Jupiter's normal modes[21].

For large atmospheric flows on rotating planets, wind shear is accompanied by density gradients; therefore, it is possible to link the flows and the gravity field directly. The velocity gradient affects both the even and odd zonal harmonic coefficients, but only the odd coefficients bear the unique signature of the dynamics when $l < 10$ (for $l > 10$ the even coefficients are also dominated by the dynamics of the flows; see Fig. 1). We singled out the contribution of the winds by removing the J_2, J_4, J_6 and J_8 harmonic components from the complete gravity potential. The north–south asymmetry component of gravity acceleration reaches its largest magnitude of 3.4 ± 0.4 mGal (3σ; 1 Gal = 1 cm s^{-2}) at a latitude of 24° N, approximately at the transition between the northern equatorial belt and the northern tropical zone (Fig. 3). Remarkably, this region corresponds to a large velocity and latitudinal gradient of surface winds, as expected for a gravity signal, owing to wind dynamics[4,14]. The odd zonal harmonics J_3, J_5, J_7 and J_9 and the associated gravity acceleration may be used to infer the depth and the vertical profile of the winds[3,4].

Online Content Methods, along with any additional Extended Data display items and Source Data, are available in the online version of the paper; references unique to these sections appear only in the online paper.

Received 20 September 2017; accepted 18 January 2018.

1. Lanzano, P. The equilibrium of a rotating body of arbitrary density. *Astrophys. Space Sci.* **29,** 161–178 (1974).
2. Hubbard, W. B. Gravitational signature of Jupiter's deep zonal flows. *Icarus* **137,** 357–359 (1999).
3. Kaspi, Y. Inferring the depth of the zonal jets on Jupiter and Saturn from odd gravity harmonics. *Geophys. Res. Lett.* **40,** 676–680 (2013).
4. Kaspi, Y. *et al.* Jupiter's atmospheric jet streams extend thousands of kilometres deep. *Nature* **555,** https://doi.org/10.1038/nature25793 (2018)
5. Guillot, T. *et al.* A suppression of differential rotation in Jupiter's deep interior. *Nature* **555,**https://doi.org/10.1038/nature25775 (2018).
6. Bertotti, B., Farinella, P. & Vokrouhlicky, D. *Physics of the Solar System: Dynamics and Evolution, Space Physics, and Spacetime Structure* 35–61 (Springer, 2012).
7. Lindal, G. F. *et al.* The atmosphere of Jupiter: an analysis of the Voyager radio occultation measurements. *J. Geophys. Res.* **86,** 8721–8727 (1981).
8. Bertotti, B., less, L. & Tortora, P. A test of general relativity using radio links with the Cassini spacecraft. *Nature* **425,** 374–376 (2003).
9. Armstrong, J. W., less, L., Tortora, P. & Bertotti, B. Stochastic gravitational wave background: upper limits in the 10^{-6} to 10^{-3} Hz band. *Astrophys. J.* **599,** 806–813 (2003).
10. Bertotti, B., Comoretto, G. & less, L. Doppler tracking of spacecraft with multifrequency links. *Astron. Astrophys.* **269,** 608–616 (1993).
11. Asmar, S. W., Armstrong, J. W., less, L. & Tortora, P. Spacecraft Doppler tracking: noise budget and accuracy achievable in precision radio science observations. *Radio Sci.* **40,** RS2001 (2004).
12. Hubbard, W. B. Effects of differential rotation on the gravitational figures of Jupiter and Saturn. *Icarus* **52,** 509–515 (1982).
13. Hubbard, W. B. & Militzer, B. A preliminary Jupiter model. *Astrophys. J.* **820,** 80 (2016).
14. Kaspi, Y., Hubbard, W. B., Showman, A. P. & Flierl, G. R. Gravitational signature of Jupiter's internal dynamics. *Geophys. Res. Lett.* **37,** L01204 (2010).
15. Bolton, S. J. *et al.* Jupiter's interior and deep atmosphere: the initial pole-to-pole passes with the Juno spacecraft. *Science* **356,** 821–825 (2017).
16. Folkner, W. M. *et al.* Jupiter gravity field estimated from the first two Juno orbits. *Geophys. Res. Lett.* **44,** 4694–4700 (2017).
17. Jacobson, R., Haw, R., McElrath, T. & Antreasian, P. A comprehensive orbit reconstruction for the Galileo prime mission. *Adv. Astronaut. Sci.* **103,** 465–486 (1999).
18. Jacobson, R. A. *Jupiter satellite ephemeris file jup310.bsp* https://naif.jpl.nasa.gov/pub/naif/generic_kernels/spk/satellites/ (2009).
19. Wahl, S. M. *et al.* Comparing Jupiter interior structure models to Juno gravity measurements and the role of an expanded core. *Geophys. Res. Lett.* **44,** 4649–4659 (2017).
20. Parisi, M. *et al.* Probing the depth of Jupiter's Great Red Spot with the Juno gravity experiment. *Icarus* **267,** 232–242 (2016).
21. Durante, D., Guillot, T. & less, L. The effect of Jupiter oscillations on Juno gravity measurements. *Icarus* **282,** 174–182 (2017).

Acknowledgements This research was carried out at the Sapienza University of Rome, University of Bologna and University of Pisa under the sponsorship of the Italian Space Agency; at the Jet Propulsion Laboratory, California Institute of Technology under a NASA contract; by the Southwest Research Institute under a NASA contract. Support was provided also by the Israeli Space Agency (Y.K. and E.G.) and the Centre National d'Études Spatiales (T.G. and Y.M.). All authors acknowledge support from the Juno Project.

Author Contributions L.I. and W.M.F. led the experiment and supervised the data analysis. L.I. wrote most of the manuscript. D.D. and M.P. carried out the gravity data analysis. Y.K. and E.G. provided models of the asymmetric and tesseral gravity field. Y.K., E.G., T.G., W.B.H. and D.J.S. carried out consistency checks with interior models and provided theoretical support. D.R.B. planned and supervised the data collection. P.R. designed and coded the orbit determination filter used in this analysis. L.G.C., P.T. and M.Z. provided the media calibrations. J.D.A., A.M., R.P. and D.S. advised on the data analysis. H.C., R.H., J.I.L., Y.M., B.M. and S.W. helped in the definition of the scientific objectives of the measurements. J.E.P.C., S.M.L. and S.J.B. supervised the planning and execution of the gravity experiment.

Author Information Reprints and permissions information is available at www.nature.com/reprints. The authors declare no competing financial interests. Readers are welcome to comment on the online version of the paper. Publisher's note: Springer Nature remains neutral with regard to jurisdictional claims in published maps and institutional affiliations. Correspondence and requests for materials should be addressed to L.I. (luciano.iess@uniroma1.it).

Reviewer Information *Nature* thanks J. Fortney and N. Nettelmann for their contribution to the peer review of this work.

METHODS

Data acquisition. Previous determinations of the Jovian gravity with Juno were carried out using the standard radio system of the spacecraft in the X band (7.2–8.4 GHz) during the first two perijove passes (PJ1 and PJ2). At these lower frequencies, Doppler data were marred by interplanetary plasma noise (although mechanical noise from the ground antenna was considerable in PJ1). Our analysis is based on radio tracking of Juno in the Ka band during two perijove transits on 11 December 2016 (PJ3 at 17:03:40 UTC; UTC, Coordinated Universal Time) and 19 May 2017 (PJ6 at 06:00:45 UTC). The use of the Ka band provided excellent immunity to propagation noises due to charged particles from solar winds and Earth's ionosphere. PJ3 and PJ6 were the first two perijove passes of the mission that were devoted to gravity science. Ground support was provided by DSS 25 (Goldstone, California), the only antenna of NASA's Deep Space Network (DSN) with two-way Ka-band capabilities. Two-way Ka- and X-band data were acquired from 12:47 UTC to 19:19 UTC during PJ3 (about 390 Doppler observables with 60 s integration time for each band), and from 01:39 UTC to 09:25 UTC (about 460 Doppler observables per band) in PJ6. To improve the estimate of the spacecraft trajectory, we also used data acquired in the X band from an antenna of the Canberra DSN complex (DSS 43) after the end of the DSS 25 pass, before an orbit-trimming manoeuvre.

Doppler data were obtained from a wide-band open-loop receiver used for radio-science investigations. A specially designed digital phase-locked loop was applied to the 1-kHz complex samples of the received electric field to obtain the phase history and the sky frequencies. Doppler data from the standard closed-loop receiver are generally noisier, resulting in larger formal uncertainties. The central values of the estimates from the two datasets are statistically compatible.

Non-gravitational accelerations. The dynamical model used in the fit is purely deterministic. All non-gravitational forces acting on the spacecraft are modelled using a suitable set of parameters, whose uncertainties contribute to the final covariance matrix. The largest non-gravitational acceleration originates from the solar radiation pressure (about 9×10^{-9} m s^{-2}) acting on the 61-m^2 solar panels and the 3-m high-gain antenna. Modelling this acceleration is simple, as the Sun aspect angle—and therefore the acceleration—is constant during the pass. We have assumed that the reflectivity of the surfaces is known with a 20% uncertainty. Our dynamical model includes the small acceleration from the latitudinally varying, Jovian infrared emission (1.2×10^{-9} m s^{-2} at the equator) and the radiation pressure from the albedo of the planet (6×10^{-10} m s^{-2}). The negligible effect of inaccurate modelling of these non-gravitational accelerations on the gravity estimate was assessed using numerical simulations. The anisotropic thermal emission from the spacecraft and from possible gas leaks may produce small additional accelerations along the direction of the spin axis (the other components are averaged out). As the direction of Earth and the Sun differ by only 9° during the observations, these accelerations can be confused with the solar radiation pressure, and their effect on the gravity estimate is accounted for in the 20% uncertainty attributed to the solar radiation pressure. Other accelerations, such as atmospheric and magnetic drag, are too small to affect the gravity estimate.

Orbit geometry. The orbit geometry is a crucial factor in gravity determinations. The key parameters are the orbital altitude and the angle between the line of sight and the spacecraft acceleration. Juno's pericentre altitudes are sufficiently low (4,154 km in PJ3 and 3,503 km in PJ6) to reveal density inhomogeneities with spatial scales much smaller than the radius of the planet. On the other hand, the large eccentricity causes the radial distance from the planet to increase quickly with latitude, strongly reducing the sensitivity to gravity disturbances in the polar regions (more markedly in the southern hemisphere, owing to the location of the pericentre north of the equator). The eccentricity of the orbit limits also the gravitational contact time: the spacecraft covers 60° in latitude in about 1,200 s, reaching a velocity of about 60 km s^{-1} at the pericentre. The other factor that affects the recovery of the gravity field is the orientation of the orbital plane with respect to Earth, which controls the projection of the spacecraft velocity along the line of sight. Although the angle between the negative orbit normal and Earth's direction is not optimal (19.2° in PJ3 and 15.1° in PJ6), the projected velocity and acceleration still provide good observability of the zonal field.

Owing to Jupiter's oblateness, the pericentre drifts northward by about 1° per orbit from an initial latitude of 2.7°. At the end of the nominal mission, it will reach a latitude of 32.6° N, allowing a better determination of gravity at high northern latitudes. The node longitude is controlled by orbital manoeuvres to target specific Jupiter longitudes and obtain uniform coverage of the planet's surface. These manoeuvres are carried out far from the pericentre and therefore do not affect the gravity determinations. The orientation of the orbital plane with respect to Earth changes from a nearly face-on configuration at orbit insertion to edge-on after about three years. Detailed information on Juno's orbit can be obtained from NASA's HORIZONS system (https://ssd.jpl.nasa.gov). Extended Data Table 1 reports the main geometrical parameters that are relevant to gravity determination.

Data quality and calibration. We have carefully assessed and ruled out considerable biases in the gravity estimate due to systematic effects in the data and the dynamical model. The largest systematic effect in the Doppler measurement is from the dry troposphere, which causes path delay variations up to about 3×10^{-4} m s^{-1} over timescales of 6–8 h. The suppression of this large signal is obtained using ground meteorological data (mostly surface pressure and temperature) and careful modelling of elevation-dependent effects. Although a small residual tropospheric signal (mostly due to horizontal pressure gradients) cannot be excluded, its timescale is much larger than that of the gravity harmonics (10–30 min). Its effect on the gravity determination is therefore negligible.

The path delay due to the ionospheric plasma is strongly reduced thanks to the use of Ka band. The DSN provides calibrations of the ionospheric path delays at each tracking complex by mapping dual-frequency GPS (Global Positioning System) measurements onto the line of sight of the spacecraft. The applied corrections never exceed a few centimetres over scales of several hours, corresponding to path delay rates of about 2×10^{-6} m s^{-1}. Although inherently small, these effects can be further reduced thanks to GPS-based calibrations.

According to models of Doppler noise in Ka-band interplanetary radio links[11], solar wind turbulence becomes a dominant noise source only at solar elongation angles lower than 15° when partial calibration aided by the X-band radio link is available[10,22]. For Juno, the expected interplanetary plasma noise in PJ3 (elongation 61.6°) and PJ6 (elongation 135.4°) is 3×10^{-7} m s^{-1} and 1×10^{-7} m s^{-1}, respectively, with 60 s integration times. These values are well below the contributions expected from the wet-troposphere path delay variation and mechanical noise from the antenna[11]. Path delay variations due to tropospheric water vapour were calibrated using two microwave radiometers located near the ground antenna, with parallel lines of sight. After these calibrations, Doppler noise at 60-s integration time decreased by about 30%.

The timescale of gravity measurements is determined by the spatial scale of the gravity field and by the spacecraft velocity. For the gravity harmonic of degree l, the timescale is roughly $\pi R/lV_{sc}$, where R is Jupiter's equatorial radius and V_{sc} is the velocity of the spacecraft near the pericentre. For $l = 12$, the timescale of the gravity signal is about 300 s. The Doppler measurements were integrated over 60 s before processing to ensure adequate sampling of the gravity signal. At this timescale, the measured range-rate noise in the Ka band was 2×10^{-5} m s^{-1} at 60 s, in line with the estimates of Ka-band radio link noise models[11]. The PJ3 and PJ6 Doppler residuals after plasma and tropospheric calibrations and the corresponding Allan deviations are shown in Extended Data Figs 1 and 2. The slope of the Allan deviation (approximately proportional to the inverse square root of the integration time) is consistent with a white Doppler noise between 4×10^{-4} and 2×10^{-2} Hz (the band of the gravity signal). The low Doppler noise experienced by Juno is much smaller than the gravity signal from the odd harmonics (an example is shown in Extended Data Fig. 3), facilitating their identification.

Replace with 1.5

Effect of the Io plasma torus. Juno's radio signal invariably crosses the region of charged particles generated by the ionization of the gases emitted by Io's volcanoes, known as the Io torus. The resulting path delay variation may be an important source of bias in the gravity estimates. The plasma density of the Io torus shows a variability of a factor of 2 over time periods of around 20 days and is difficult to model[23]. The path delay variation during a Juno pass can be estimated and partially calibrated by means of differential Doppler measurements in the X and Ka bands. In PJ3 and PJ6, we measured path delay variations ascribed to the Io torus of about 2–4 cm in the Ka band (16 times larger in the X band) over a time period of about two hours.

The fractional frequency shift y of the received signal can be modelled as the sum of a non-dispersive contribution y_{nd} (dominated by the orbital dynamics) and a dispersive contribution from charged particles:

$$y = y_{nd} + k\left(\frac{\dot{P}_u}{f_u^2} + \frac{\dot{P}_d}{\alpha^2 f_u^2} + \frac{\dot{I}_u}{f_u^2} + \frac{\dot{I}_d}{\alpha^2 f_u^2}\right) \quad (1)$$

Here f_u is the frequency of the signal transmitted by the ground station and α is the transponding ratio (the ratio between the frequencies transmitted and received by the spacecraft). $\dot{P}_u$, $\dot{P}_d$, $\dot{I}_u$ and $\dot{I}_d$ are the time derivatives of the columnar electron content from the interplanetary and ionospheric plasma and the Io torus, respectively, in the uplink (subscript 'u') and downlink ('d') paths. The constant $k = e^2/(8\pi^2\varepsilon_0 m_e c)$ is approximately 1.34×10^{-7} m^2 s^{-1}, where e and m_e are the charge and mass of the electron, respectively, ε_0 is the vacuum permittivity and c is the speed of light in vacuum. When multiple frequencies are available, the dispersive terms can be fully or partially measured thanks to the frequency dependence of the plasma refractive index[10,22].

Owing to the difference in the transponding ratios of the X band and the Ka band (880/749 and 3,360/3,599, respectively), the overall plasma contribution in PJ3 and PJ6 can be estimated to 75% accuracy[10]. Under the assumption $\dot{I}_u = \dot{I}_d$

(which has been verified because the Io torus is only 1.5 light-seconds away from Juno), the frequency shift due to the Io torus is obtained by differencing the relative frequency shift of the X and Ka bands, which is described by equation (1):

$$k\left(\frac{1}{f_{\mathrm{K}}^2}+\frac{1}{\alpha_{\mathrm{K}}^2 f_{\mathrm{K}}^2}\right)\dot{I}=\left(\frac{f_{\mathrm{K}}^2}{f_{\mathrm{X}}^2}\frac{\alpha_{\mathrm{K}}^2}{\alpha_{\mathrm{X}}^2}\frac{\alpha_{\mathrm{X}}^2+1}{\alpha_{\mathrm{K}}^2+1}-1\right)^{-1} \left\{y_{\mathrm{X}}-y_{\mathrm{K}}-k\left[\dot{P}_{\mathrm{u}}\left(\frac{1}{f_{\mathrm{X}}^2}-\frac{1}{f_{\mathrm{K}}^2}\right)+\dot{P}_{\mathrm{d}}\left(\frac{1}{\alpha_{\mathrm{X}}^2 f_{\mathrm{X}}^2}-\frac{1}{\alpha_{\mathrm{K}}^2 f_{\mathrm{K}}^2}\right)\right]\right\} \quad (2)$$

In equation (2), the estimated Io torus signal is contaminated by the uplink and downlink interplanetary plasma variations in the columnar electron content. In the PJ3 and PJ6 data, we observed a residual plasma noise of about 8×10^{-7} m s^{-1} (relative frequency shift 2.7×10^{-15}) for 60 s integration time. We assessed the effect of this error by means of numerical simulations.

Simulated Doppler observables of PJ3 and PJ6 were generated using the same dynamical model adopted in the analysis of the PJ3 and PJ6 data. A white Gaussian noise with a standard deviation equal to the observed one was added to the simulated observables. Then, we added a signal that mimics the effect of the Io torus to the simulated Doppler observables using a simple Gaussian model for the path delay Δl on a signal of frequency f:

$$\Delta l=\Delta l_{\mathrm{K}}\left(\frac{f_{\mathrm{K}}}{f}\right)^2\exp\left[-\frac{1}{2}\left(\frac{t-\Delta\tau}{\tau/6}\right)^2\right] \quad (3)$$

Here Δl_{K} is the maximum path delay on a signal with frequency f_{K}, τ is the total duration of the torus signal (corresponding to 6 standard deviations of a Gaussian curve), and $\Delta\tau$ is the delay between the time of the maximum path delay and the orbit pericentre. The values of the parameters adopted for each flyby were derived from direct measurements carried out in PJ3 and PJ6. PJ3 (PJ6) observations gave the values $\Delta l_{\mathrm{K}}=2.1$ cm (4.6 cm), $\tau=120$ min (150 min) and $\Delta\tau=-15$ min ($+10$ min). The fractional frequency shift Δy on the Doppler observables is given by:

$$\Delta y=\frac{\Delta l}{c}=-\left(\frac{f_{\mathrm{X}}}{f}\right)^2\frac{\Delta l_{\mathrm{K}}}{c\tau/6}\frac{t-\Delta\tau}{\tau/6}\exp\left[-\frac{1}{2}\left(\frac{t-\Delta\tau}{\tau/6}\right)^2\right] \quad (4)$$

To simulate the calibration error due to the residual plasma noise in equation (2), the calibrations were generated using the same model, but by perturbing the input parameters with white, Gaussian random values. The standard deviations of the perturbing terms were chosen to match the observed solar plasma noise. The resulting standard deviation δ of the path delay was less than 10%.

We then carried out a Monte Carlo simulation using 1,000 noise realizations and obtained a sample of estimated gravity fields. None of the gravity harmonic coefficients changed by more than 1σ (Extended Data Figs 4 and 5). By contrast, the Io torus can cause biases up to about 5σ on gravity solutions based on X-band data. The most affected gravity coefficients are J_2, J_3 and J_4.

Tesseral gravity field. The solution reported in Table 1 includes only degree-2 tesseral gravity harmonics. Although higher-degree tesseral harmonics are not required to fit the data to the noise level, a higher-degree field is certainly present. To assess the effect of a tesseral field on the actual estimate, simulations with synthetic Doppler data were conducted. Thermal wind models with a scale height of 1,900 km (which is consistent with the observed odd harmonics[3]) but with a different scale height for the vortices (associated with the tesseral component), were used to generate synthetic gravity fields. The resulting simulated Doppler observables were fitted with the dynamical model used to obtain our solution (Table 1), limited to degree-2 tesseral harmonics. Our goal was to identify the largest tesseral field (and therefore the largest scale height) that can be hidden in the Doppler data without producing signatures in the residuals. We found that the threshold value of the scale height is about 380 km.

To include the effect of the neglected tesseral field in the estimation, we performed a consider analysis, which quantifies the effect of non-estimated parameters (the higher-degree tesseral field) on the uncertainties of the estimated parameters. The analysis revealed that inclusion of the tesseral field increases these uncertainties. Extended Data Table 2 presents the consider uncertainties of the estimate for a thermal wind model with a vortex scale height of 380 km.

Data availability. The Juno tracking data and the ancillary information used in this analysis are archived at NASA's Planetary Data System (https://pds.nasa.gov).

Code availability. The analysis presented in this work relies on proprietary orbit determination codes that are not publicly available. The MONTE software package is used at the Jet Propulsion Laboratory for planetary spacecraft navigation. The ORACLE orbit determination filter was developed at Sapienza University of Rome under contract with the Italian Space Agency.

22. Mariotti, G. & Tortora, P. Experimental validation of a dual uplink multifrequency dispersive noise calibration scheme for deep space tracking. *Radio Sci.* **48,** 111–117 (2013).
23. Delamere, P. A. & Bagenal, F. Modeling variability of plasma conditions in the Io torus. *J. Geophys. Res. Space Phys.* **108,** 1276 (2003).
24. Seidelmann, P. K. & Divine, N. Evaluation of Jupiter longitudes in System III (1965). *Geophys. Res. Lett.* **4,** 65–68 (1977).

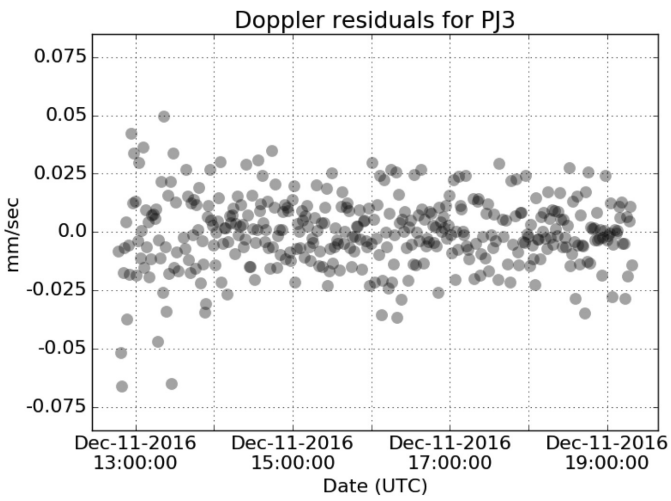

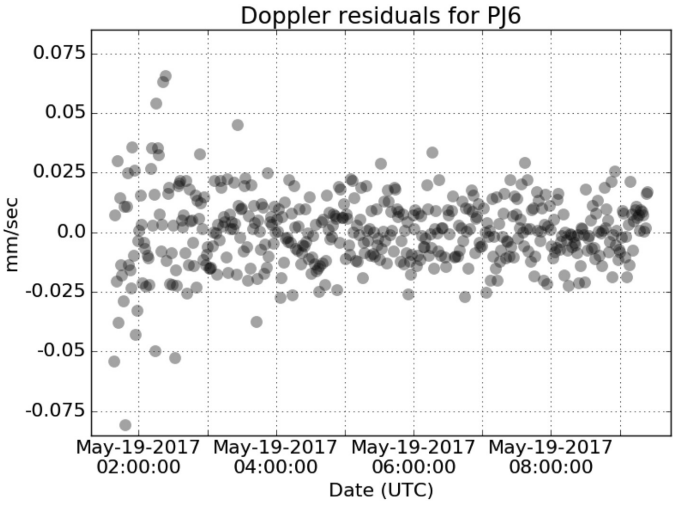

Extended Data Figure 1 | Range-rate residuals. Two-way range-rate residuals (integrated over 60 s) for the Ka-band perijove passes PJ3 and PJ6 are shown. The root-mean-square value of the residuals is 0.015 mm s^{-1} for both passes. The measured range rate was obtained from the radio-science open-loop receiver.

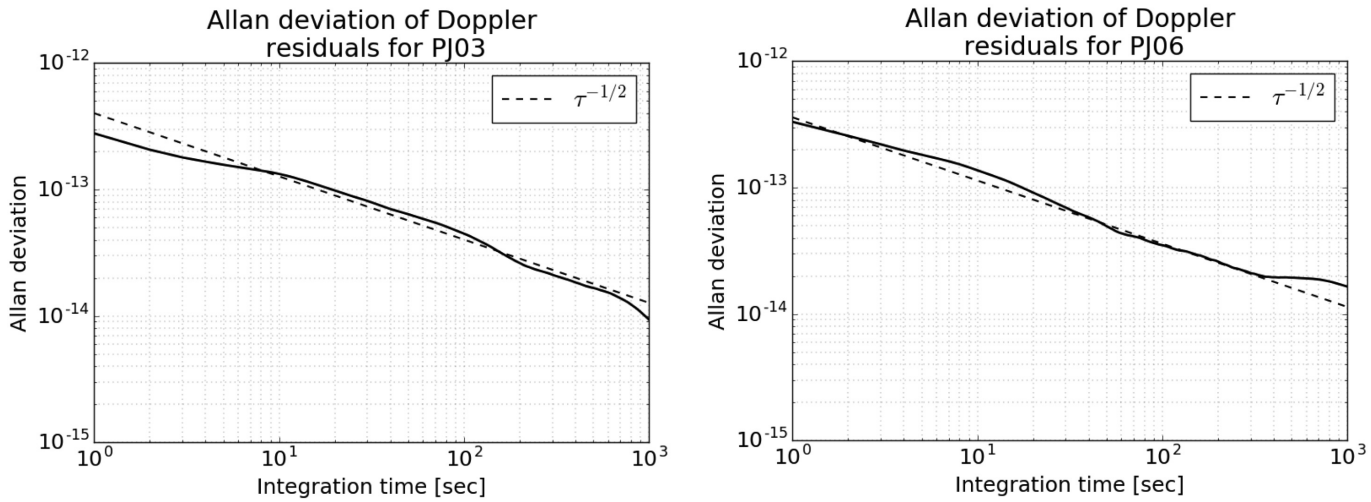

Extended Data Figure 2 | Frequency stability. The Allan deviation of relative frequency shift for the Ka-band perijove passes PJ3 and PJ6 is shown. The slopes are roughly consistent with white noise (dashed line).

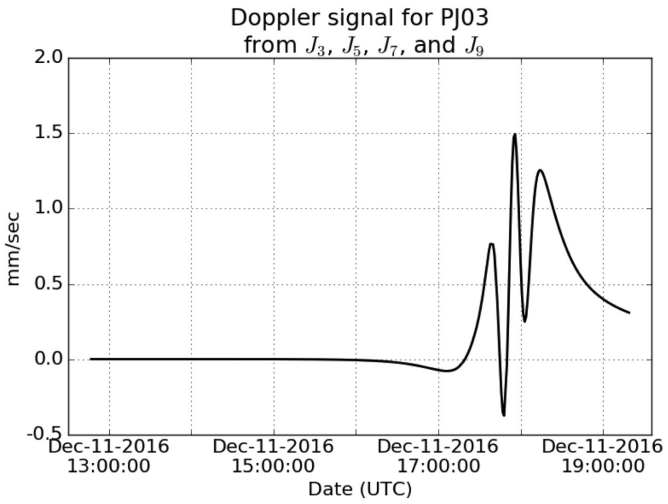

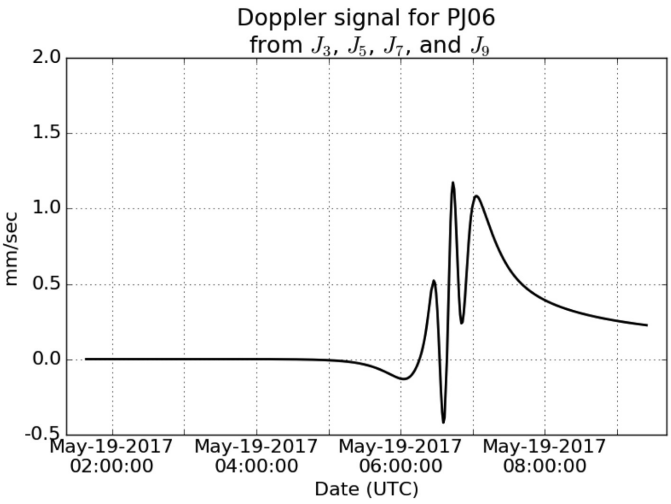

Extended Data Figure 3 | Gravity harmonic signatures. Range-rate signals from the J_3, J_5, J_7 and J_9 gravity harmonics for PJ3 and PJ6 are shown. The smaller signal in PJ6 is due to a less favourable projection of the spacecraft velocity along the Earth–Jupiter line of sight (the angle between Juno's orbit normal and the line of sight was 19.2° in PJ3 and 15.1° in PJ6). By comparison, the range-rate noise at 60 s is 0.015 mm s^{-1} in both passes.

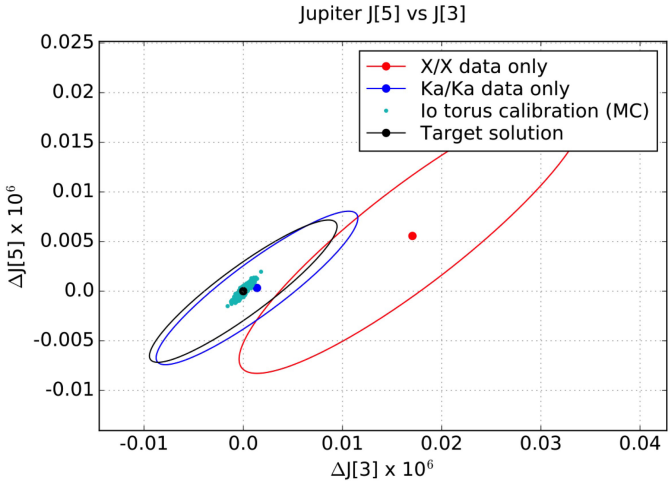

Extended Data Figure 4 | Io torus effects on the estimation of J_3–J_5. Shown are estimation biases on J_3 and J_5 due to calibration errors of the Io torus path delay variation (cyan dots) in a Monte Carlo (MC) simulation of passes PJ3 and PJ6 of the Juno gravity experiment. The calibration errors are compared to the estimated 3σ uncertainty ellipses of the target solution (black), obtained without the Io torus, and the solutions obtained using only X- (red) and Ka-band (blue) data. The estimation bias on J_3 is about 3σ if X-band data are used. Ka-band data or dual-link calibration reduce the bias to less than 1σ.

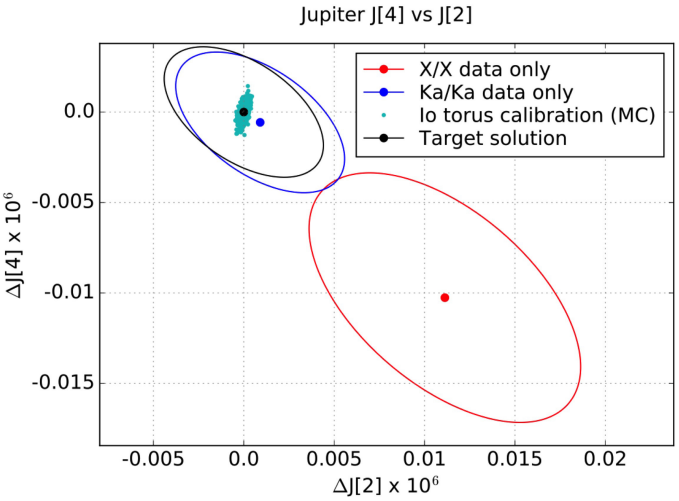

Extended Data Figure 5 | Io torus effects on the estimation of J_2–J_4. Shown are estimation biases on J_2 and J_4 from the Monte Carlo simulation, as in Fig. 1. The estimation bias on J_2 and J_4 is larger than 4σ if X-band data are used, while using Ka-band or plasma-calibrated data reduces it to less than 1σ.

Extended Data Table 1 | Characteristics of perijove passes PJ3 and PJ6 used in the gravity solution

	PJ3	PJ6
Perijove epoch	11-DEC-2016 17:03:41 UTC	19-MAY-2017 06:00:44 UTC
One-way light-time	2924 s	2339 s
Perijove latitude	5.7°	8.5°
Perijove altitude	4154 km	3503 km
Sun-Earth-Probe angle	61.6°	135.4°
NON to Earth angle	19.2°	15.1°
Longitude at equator crossing	6.8°	142.0°

Altitude refers to the oblate planet. The negative orbit normal (NON) to Earth is the angle between the opposite of the orbit normal and Earth's direction. Longitude at equator crossing refers to System III[24].

Extended Data Table 2 | Consider analysis covariances (3σ)

	Value	Uncertainty	Consider uncertainty
J_2 ($x10^6$)	14696.572	0.014	0.024
C_{21} ($x10^6$)	-0.013	0.015	0.018
S_{21} ($x10^6$)	-0.003	0.026	0.035
C_{22} ($x10^6$)	0.000	0.008	0.023
S_{22} ($x10^6$)	0.000	0.011	0.046
J_3 ($x10^6$)	-0.042	0.010	0.024
J_4 ($x10^6$)	-586.609	0.004	0.008
J_5 ($x10^6$)	-0.069	0.008	0.013
J_6 ($x10^6$)	34.198	0.009	0.012
J_7 ($x10^6$)	0.124	0.017	0.024
J_8 ($x10^6$)	-2.426	0.025	0.026
J_9 ($x10^6$)	-0.106	0.044	0.061
J_{10} ($x10^6$)	0.172	0.069	0.070
J_{11} ($x10^6$)	0.033	0.112	0.148
J_{12} ($x10^6$)	0.047	0.178	0.178
k_{22}	0.625	0.063	0.118
RA (deg)	268.0570	0.0013	0.0052
Dec (deg)	64.4973	0.0014	0.0067

Consider uncertainties are shown after a tesseral field corresponding to a flow depth of 380 km is added to the estimated zonal field in Table 1. Gravity fields generated by larger depths of the tesseral flow would produce signatures in the Doppler residuals[20].